Organic–Inorganic Copper Halide Compound with a Near-Unity Emission Large-Scale Synthesis and Diverse Light-Emitting Applications

Chen, Kunlin; Chen, Bingkun; Xie, Lingling; Li, Xitao; Chen, Xiyao; Lv, Ning; Zheng, Kun; Liu, Zhe; Pi, Huihui; Lin, Zhengguo; Rogach, Andrey L.

Published in:
Advanced Functional Materials

Published: 04/03/2024

Document Version:
Post-print, also known as Accepted Author Manuscript, Peer-reviewed or Author Final version

Published version (DOI):
10.1002/adfm.202310561

Publication details:
Chen, K., Chen, B., Xie, L., Li, X., Chen, X., Lv, N., Zheng, K., Liu, Z., Pi, H., Lin, Z., & Rogach, A. L. (2024). Organic–Inorganic Copper Halide Compound with a Near-Unity Emission: Large-Scale Synthesis and Diverse Light-Emitting Applications. *Advanced Functional Materials*, *34*(10), Article 2310561. https://doi.org/10.1002/adfm.202310561

Organic-Inorganic Copper Halide Compound with a Near-Unity Emission: Large-Scale Synthesis and Diverse Light-Emitting Applications

Kunlin Chen, Bingkun Chen, Lingling Xie, Xitao Li, Xiyao Chen, Ning Lv, Kun Zheng, Zhe Liu, Huihui Pi, Zhengguo Lin*, Andrey L. Rogach**

K. Chen, B. Chen, L. Xie, X. Li, X. Chen, N. Lv, K. Zheng, Z. Liu, H. Pi
Beijing Engineering Research Center of Mixed Reality and Advanced Display, School of Optics and Photonics, Beijing Institute of Technology, Beijing 100081, P. R. China
Z. Lin
College of Chemistry and Materials Science, Hebei Normal University, Shijiazhuang 050024, P. R. China
A. L. Rogach
Department of Materials Science and Engineering, and Centre for Functional Photonics (CFP), City University of Hong Kong, Hong Kong SAR 999077, P. R. China
Email: chenbk@bit.edu.cn
Email: linzhengguo11@163.com
Email: andrey.rogach@cityu.edu.hk

Keywords: organic-inorganic copper halides, self-trapped excitons, white light-emitting devices, scintillators, luminescent inks

Abstract

Low-dimensional organic-inorganic metal halides (OIMHs) have emerged as promising light emitters due to their broadband emission originating from self-trapped excitons (STE), especially for Cu-based OIMHs. Herein, Cu(I)-based OIMH with a structure of $(TPP)_2Cu_4I_6 \cdot 2DMSO$ (TPP stays for tetraphenylphosphonium, and DMSO – for dimethyl sulfoxide) has been synthesized, both in form of single crystals and as a microcrystalline powder. This compound exhibits a broadband green emission with a peak at 515 nm and a full width at half-maximum of 78 nm, and a near-unity photoluminescence quantum yield of 99.5%. Experimental data supported by theoretical calculations indicate that the STE emission is responsible for the green emission with a long lifetime of 2.53 μs. Down-conversion light-emitting device with a high luminous efficiency of 50 lm W^{-1} based on this compound have been fabricated, and white light has also been achieved with a high color rendering index of

96.7. Moreover, green emissive $(TPP)_2Cu_4I_6 \cdot 2DMSO$ was utilized in scintillators for X-ray detection and imaging, and as a luminescent ink for encryption applications.

TOC text

We synthesized a novel Cu(I)-based organic-inorganic halide compound $(TPP)_2Cu_4I_6 \cdot 2DMSO$, which exhibits broadband green emission with a near-unity photoluminescence quantum yield; self-trapped excitons are responsible for this emission. This compound was used for fabrication of down-conversion white LEDs, X-ray scintillators and luminescent inks.

TOC figure

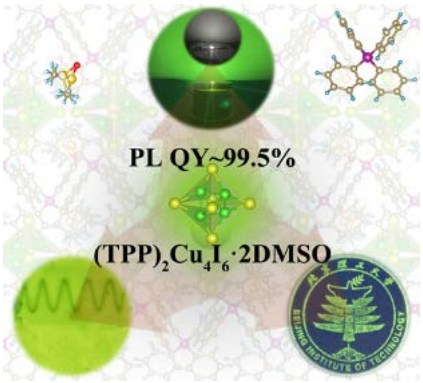

1. Introduction

In recent years, among various functional materials,[1] organic-inorganic metal halides (OIMHs) have experienced impressive progress with a view of a broad range of optoelectronic device applications, such as solar cells,[2] light-emitting diodes,[3] and photodetectors.[4] Especially, Cu(I)-based OIMHs have emerged as promising luminescent materials, due to their low toxicity, low cost and earth-abundance of the precursor materials.[5] It is noteworthy that these compounds are highly emissive without the need of additional doping, alloying, etc.[6] Moreover, their syntheses can be conducted under mild reaction conditions, thus rendering those compounds more sustainable and environmentally friendly. The selection of organic constituents plays a pivotal role in tailoring the optical properties of Cu-based OIMHs, with $Cu_xI_y(ligand)_z$ hybrid materials been broadly investigated.[7] At the same time, the synthesis of organic ligands increases the complexity of those compounds, and could limit the feasibility of their large-scale production. Recently, OIMHs with inclusion of dimethyl sulfoxide (DMSO) as organic species within their crystal lattice have been introduced.[8] The coordinative bonds between the DMSO and alkali metal cations or organic cations lead to formation of a so-called zero-dimensional (0D) structure, where metal halide polyhedra are surrounded and isolated by large organic cations, which results in their better stability and stronger exciton confinement as compared to 3D metal halides.[9] It has been reported that 0D OIMHs possess large exciton binding energy, high photoluminescence quantum yields (PL QYs), and large Stokes shift between the absorption and emission bands.[10] $RbCu_2I_3$·DMSO showed green emission with PL QY of 38.2%,[11] while $K_6(DMSO)_{12}[Cu_8Br_{13}][Cu_4Br_4(OH)(H_2O)]$ displayed red emission with PL QY of 74.8%.[12] Still, stability of these compounds can be impacted by air and continuous UV irradiation, leading to their decomposition owing to the loss of DMSO molecules. One approach towards improving the stability would be to strengthen the bond with DMSO molecules by incorporating suitable organic cations, as was confirmed by several studies.[8a, 13]

Here, we combined tetraphenylphosphonium (TPP^+) cation and DMSO to synthesize a novel Cu(I)-based OIMH compound $(TPP)_2Cu_4I_6$·2DMSO. Under excitation at 365 nm, it experienced a broadband green emission with a peak at 515 nm and extremely high PL QY reaching 99.5%, which is the highest value among any similar compounds containing DMSO (see Table S1, Supporting Information). Based on experimental data and theoretical calculations, we ascribed its emission to the self-trapped excitons (STE) caused by the distortion of $[Cu_4I_6]^{2-}$ polyhedra. The hydrogen bonds formed between the oxygen atoms of DMSO and

the hydrogen atoms of TPP^+ conferred remarkable stability to this compound, both when stored under air and under UV light irradiation. To explore the practical applications of $(TPP)_2Cu_4I_6 \cdot 2DMSO$, down-conversion white light-emitting devices (WLEDs) and scintillators for X-ray detection have been demonstrated. Moreover, we also utilized this compound for security applications, processing it into a luminescent ink for encryption purposes.

2. Results and Discussion

2.1. Synthesis and Crystal Structure

Single crystals of $(TPP)_2Cu_4I_6 \cdot 2DMSO$ were produced by cooling crystallization method,[14] and $(TPP)_2Cu_4I_6 \cdot 2DMSO$ microcrystalline powder was prepared via a one-step antisolvent method followed by filter membrane-assisted post-processing at room temperature under ambient atmosphere, as illustrated in **Figure 1**a. The latter strategy allowed us to produce this compound in a quantity of up to 1 g in a single run, as shown by a photograph in Figure 1b. Full details of the synthetic procedures can be found in the Experimental Section. While adjusting the molar ratios (1:1, 1:1.5 and 1:2) of the TPPI and CuI, we have found that the best quality of the $(TPP)_2Cu_4I_6 \cdot 2DMSO$ product was achieved for the molar ratio of 1:1.5. In the synthesis of single crystals, a byproduct of $TPPI_3$ was observed when the 1:2 molar ratio was used, while for the powdered sample formation of $(TPP)_2Cu_2I_4$ phase was observed for the molar ratio of 1:1, as identified by the powder X-ray diffraction (PXRD) analysis (Figure S1a, Supporting Information). In addition, Cu^+ was partially oxidized into Cu^{2+} after a few days, which was confirmed by the X-ray photoelectron spectroscopy (XPS) with the satellite peak of Cu^{2+} observed at 944.4 eV when the molar ratio of 1:2 was employed for producing the powdered sample (Figure S2, Supporting Information). The same trends appeared in samples when the molar ratios lower than 1:2 were utilized. At the same time, the powder synthesized with a 1:1.5 molar ratio of TPPI and CuI demonstrated the best stability (Figure S1b) and the highest PL QY of 99.5%. Thus, this molar ratio 1:1.5 has been used to produce the high-quality $(TPP)_2Cu_4I_6 \cdot 2DMSO$ samples which will be considered in the subsequent discussion.

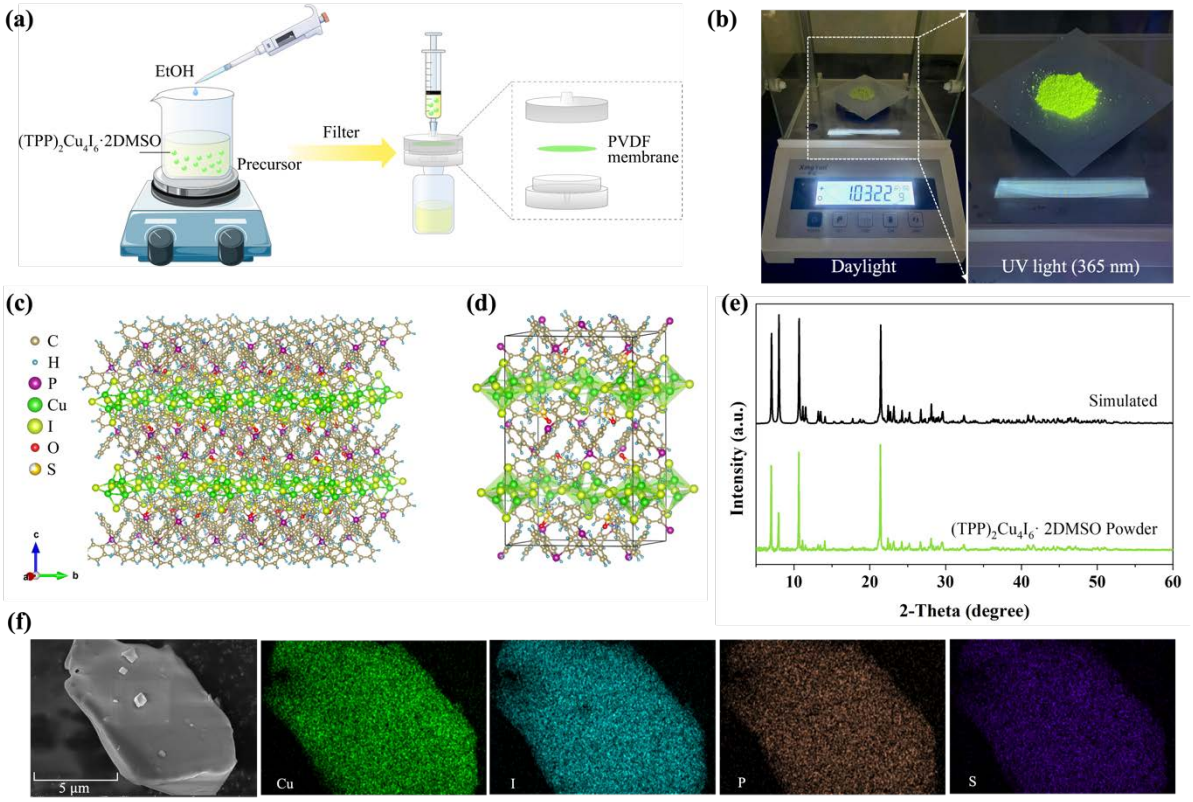

Figure 1. (a) Schematics of the fabrication process of $(TPP)_2Cu_4I_6$·2DMSO powder by antisolvent method and filter membrane-assisted post-processing. (b) Photographs of the $(TPP)_2Cu_4I_6$·2DMSO powder (~1 g) taken under daylight (left) and UV light (right). (c) Crystal structure of $(TPP)_2Cu_4I_6$·2DMSO. (d) Unit cell of $(TPP)_2Cu_4I_6$·2DMSO. (e) Experimental powder XRD pattern, and simulated single crystal XRD pattern of $(TPP)_2Cu_4I_6$·2DMSO. (f) SEM image of a piece of $(TPP)_2Cu_4I_6$·2DMSO powder, with respective elemental mapping images of Cu, I, P and S elements.

Another vital aspect to consider during the antisolvent synthesis process is the control of the antisolvent to solvent ratio. We have changed the ratio of ethyl alcohol (EtOH) to DMSO in the range from 1:1 to 8:1, and found out the ratios between 2:1 and 5:1 to be the optimal. When the amount of antisolvent was insufficient (for the ratios below 5:1), the reaction product was difficult to precipitate, while employing an excessive amount of antisolvent led to partial degradation of the resulting green luminescent material into the non-luminous substance (Figure S3, Supporting Information).

Crystal structure of $(TPP)_2Cu_4I_6$·2DMSO was determined by single-crystal X-ray diffraction analysis. It revealed that the product crystallized in the orthorhombic lattice with a space group *Pbcn*, and the cell parameters a = 15.33 Å, b = 15.85 Å, c = 25.11 Å, V = 6100.89 Å^3 (Table S2, Supporting Information). Tables S3-S6 of the Supporting Information further listed the

atomic coordinates, displacement parameters, bond lengths and bond angles. The $[Cu_4I_6]^{2-}$ unit consists of a Cu_4 tetrahedron with six coordinated I^-, which is surrounded by large organic cation TPP^+ and DMSO molecules via electrostatic interaction and hydrogen bonding interaction (Figure 1c, d). Each copper atom binds to three iodine atoms forming trigonal planar $[CuI_3]^-$ unit, while $[Cu_4I_6]^{2-}$ polyhedron is composed of four trigonal planar $[CuI_3]^-$ units by iodine-sharing. Both the peaks and intensities of the powder XRD pattern of $(TPP)_2Cu_4I_6{\cdot}2DMSO$ matched with those of the simulated XRD pattern of single crystals (Figure 1e), indicating that the powder sample exhibited high crystal quality. From the energy dispersive spectrometry (EDS) analysis performed on a piece of the $(TPP)_2Cu_4I_6{\cdot}2DMSO$ powder whose scanning electron microscope (SEM) image is shown on the left of Figure 1f, the contents of P, S, Cu and I elements have been determined as 14%, 14%, 29% and 43%, respectively, which translates into the P:S:Cu:I molar ratio of 2.0:2.1:4.1:6.1 being close to the anticipated 2:2:4:6 stoichiometry of the $(TPP)_2Cu_4I_6{\cdot}2DMSO$ compound. Mapping images for P, Cu, I and S elements uniformly distributed over the $(TPP)_2Cu_4I_6{\cdot}2DMSO$ microcrystal are presented in Figure 1f.

XPS analysis was further used to confirm the existence and valence state of the constituting elements (Figure S4, Supporting Information). The high-resolution spectrum of Cu 2p shows a doublet at 932.2 eV and 952.0 eV, signifying contributions from Cu $2p_{3/2}$ and Cu $2p_{1/2}$, respectively. The gap of 19.8 eV between the two peaks is a discernible feature of Cu^+.[15] Notably, the non-existence of the satellite peak around 943.0 eV is indicative of the absence of Cu^{2+} in the sample. The high-resolution XPS spectrum of I 3d shows two peaks at 618.9 eV ($3d_{5/2}$) and 630.4 eV ($3d_{3/2}$) with an interval of 11.5 eV, and P 2p spectrum displays a doublet around 133 eV, as illustrated in Figure S4c and d, which is coincident with I^- and P^{5+}.[16]

The actual amount of the constituting chemical elements in the sample was quantified using highly sensitive analytical techniques: organic elemental analysis (EA), inductively coupled plasma optical emission spectrometry (ICP-OES), and inductively coupled plasma mass spectrometry (ICP-MS), with the obtained results summarized in Table 1. One can see that the determined mass fractions and the resulting molar ratios of C, H, P, S, Cu and I elements in the studied compound are in good accordance with the calculated mass fractions and the stoichiometry molar ratios assuming the chemical formula $(TPP)_2Cu_4I_6{\cdot}2DMSO$. These observations also confirm that the samples are free from significant impurities or contamination, further confirming the successful synthesis of the $(TPP)_2Cu_4I_6{\cdot}2DMSO$ compound.

Table 1. Elemental content for the $(TPP)_2Cu_4I_6$·2DMSO powder, estimated by several measurement techniques (EA, ICP-OES, ICP-MS)

Element	Methods	Actual concentration (mg kg^{-1})	Mass fraction (%)	Calculated mass fraction (%)	Molar ratio
C	EA	-	33.67	33.73	C:H:P:S:Cu:I = 26:25:1:1:2:3
H	EA	-	2.79	2.81	
P	ICP-OES	33331.90	3.33	3.35	
S	ICP-OES	33105.05	3.31	3.46	
Cu	ICP-MS	136670.42	13.67	13.73	
I	ICP-MS	424703.63	42.47	41.19	

The Fourier transform infrared (FTIR) spectrum shown in Figure S5 (Supporting Information) revealed that $(TPP)_2Cu_4I_6$·2DMSO powder exhibits distinctive peaks at 1434.02 cm^{-1}, 1107.74 cm^{-1} and 723.17 cm^{-1}, which can be attributed to C-H bending, rocking, and wagging vibrations, respectively. Peaks at 688.74 cm^{-1} and 526.62 cm^{-1} correspond to C−H scissoring and C−C breathing vibration, respectively. The peak observed at 751.02 cm^{-1} can be associated with the C-P asymmetrical stretching vibration, and the peak at 1045.57 cm^{-1} is ascribed to the S=O stretching vibration. These FTIR features are consistent with those reported for similar compounds such as $(TPP)_2Cu_2I_4$ and $K_6(DMSO)_{12}[Cu_8Br_{13}][Cu_4Br_4(OH)(H_2O)]$,[12, 17], and provide additional insights into the chemical composition and structural characteristics of the sample. In particular, the S=O stretching vibrations confirms the presence of DMSO molecules as inclusions in the fabricated compound. Thermogravimetric analysis (TGA) shown in Figure S6 revealed that the $(TPP)_2Cu_4I_6$·2DMSO powder starts to degrade at 84.2 °C, which is most probably associated with dissociation of DMSO molecules because of the weight loss of 8.6% (theoretically it would be 8.4%). The powder lost 50.2% (theoretical value would be 50.4%) of its initial mass in the second stage, corresponding to the degradation of TPPI, while the last stage showed a mass loss of 39.3% (the expected value would be 41.2%) which can be attributed to the degradation of CuI. These results well coincide with the proportion of DMSO, TPPI and CuI in anticipated $(TPP)_2Cu_4I_6$·2DMSO composition.

2.2 Optical Properties and Electronic Structure

UV-vis diffuse reflection spectrum of the $(TPP)_2Cu_4I_6$·2DMSO powder was measured and subsequently converted into absorption spectrum using the Kubelka-Munk function (Figure S7, Supporting Information). The resulting spectrum shows two broad absorption peaks at around 430 nm and 720 nm. Based on the Tauc plot analysis, the bandgap of the $(TPP)_2Cu_4I_6$·2DMSO

powder is estimated to be 2.43 eV, corresponding to green light emission. Indeed, also $(TPP)_2Cu_4I_6$·2DMSO single crystals emit green light upon 365 nm UV light irradiation (Figure S8, Supporting Information). The PL spectrum of the $(TPP)_2Cu_4I_6$·2DMSO powder is shown in **Figure 2**a, demonstrating a broad emission band extending across the wavelength range of 450-650 nm with a peak at 515 nm, a full width at half maximum (FWHM) of 78 nm, and a large Stokes shift of 85 nm. There are three peaks in the broad photoluminescence excitation (PLE) spectrum at 282 nm, 370 nm and 442 nm. PL QY of the powdered sample is high, reaching 99.5% under 365 nm excitation at room temperature (Figure S9a, Supporting Information), which is one of the most efficient green emitters ever reported[18] and much higher than that of $(TPP)_2Cu_2I_4$ phase (Table S7, Supporting Information). The time-resolved PL spectrum for the $(TPP)_2Cu_4I_6$·2DMSO powder monitored at 515 nm at room temperature is shown in Figure 2b, providing a single-exponential decay with a long lifetime of 2.53 μs, which is comparable to other Cu-based OIMHs.[19] These optical properties, including microsecond decay lifetime, high PL QY, large Stokes shift and broad emission band suggest that the presence of self-trapped emitting centers, as will be confirmed later on.

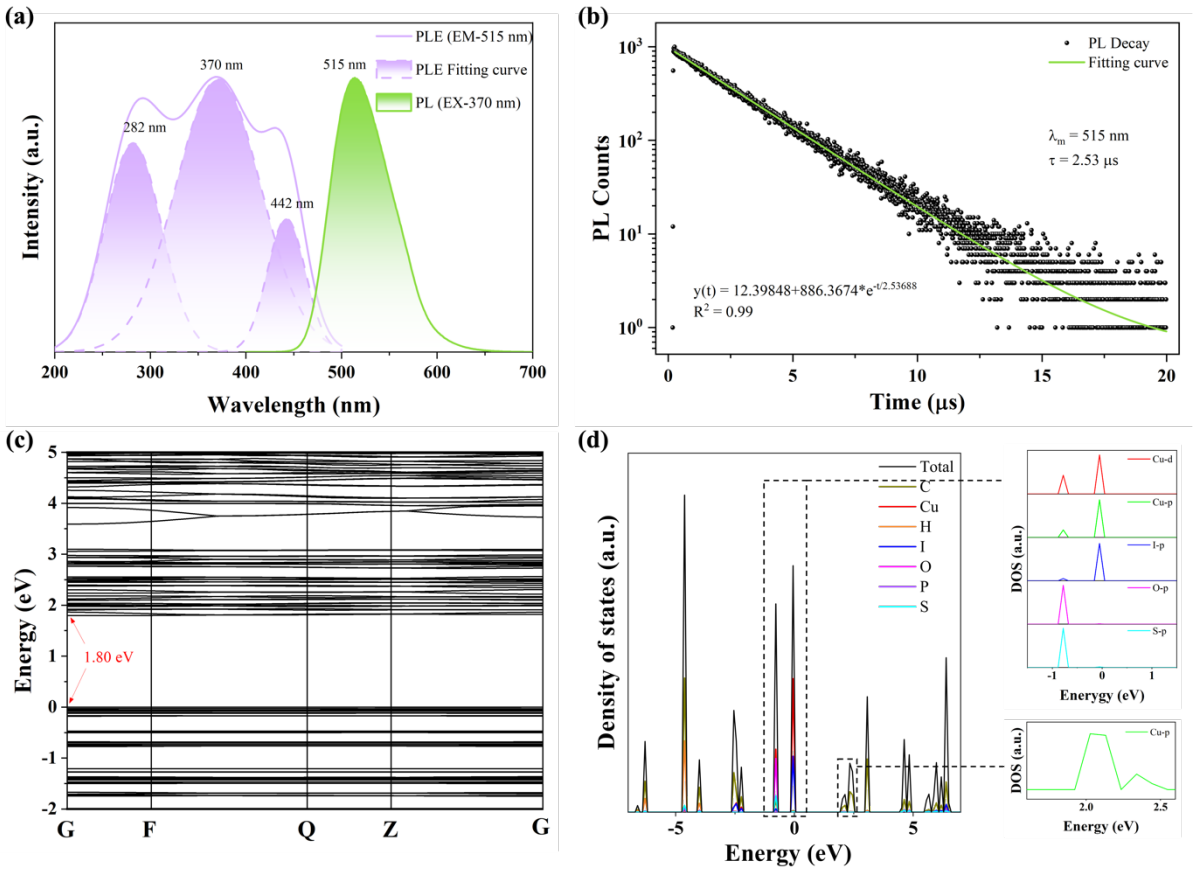

Figure 2. (a) Experimental data and fitting Gaussian curves of PLE (λ_{em} = 515 nm) and PL (λ_{ex} = 370 nm) spectra of the $(TPP)_2Cu_4I_6$·2DMSO powder. (b) Time-resolved PL decay (black

symbols), and a single-exponential fitting curve (green line) for the $(TPP)_2Cu_4I_6{\cdot}2DMSO$ powder. (c) Electronic band structure of $(TPP)_2Cu_4I_6{\cdot}2DMSO$ calculated by DFT. (d) DFT calculated total and projected DOS of $(TPP)_2Cu_4I_6{\cdot}2DMSO$, and Cu-p, Cu-d, I-p, O-p and S-p contributions to DOS.

We collected PLE spectra of the $(TPP)_2Cu_4I_6{\cdot}2DMSO$ powder monitored at various emission wavelengths, and PL spectra under different excitation wavelengths, with the data provided in Figure S10 (Supporting Information). PLE spectra probed at various emission wavelengths (495-545 nm) exhibit similar shapes, indicating existence of three different distinct transition channels from the ground state to the excited states. PL spectra show almost the same spectral shape under different excitation wavelengths (275-450 nm), pointing out the excitation independent characteristics. Moreover, the linear dependence of the emission intensity on varying excitation power (Figure S11, Supporting Information) rules out the possibility of emission caused by defects, since such defects would lead to saturation of the PL intensity at high excitation power.[20]

To gain insights into the electronic structure of $(TPP)_2Cu_4I_6{\cdot}2DMSO$, we utilized a plane-wave projector-augmented wave (PAW) implementation of density functional theory (DFT), which was executed through the Vienna Ab initio Simulation Package (VASP) software package, to compute its density of states (DOS). The results of the DFT calculations are presented in Figure 2c, revealing the existence of direct bandgap occurring at G point in the electronic structure of $(TPP)_2Cu_4I_6{\cdot}2DMSO$. The calculated bandgap is equal to 1.80 eV, which is significantly lower than the experimental one of 2.43 eV obtained from the Tauc plot (inset of Figure S7, Supporting Information). Such an underestimation of the bandgap value is a well-known phenomenon associated with DFT calculations.[21] The valence band and the conduction band of $(TPP)_2Cu_4I_6{\cdot}2DMSO$ are nearly flat, indicating a strong confinement effect, which is a characteristics of 0D OIMHs.[22] The total and projected DOS of $(TPP)_2Cu_4I_6{\cdot}2DMSO$ (Figure 2d) reveal that the valence band maximum (VBM) is mainly contributed by Cu-d, Cu-p and I-p orbitals, while Cu-p orbital also contributes to the conduction band minimum (CBM). Both O-p and S-p orbitals exhibit negligible contributions to CBM and VBM, suggesting that DMSO molecules do not influence the electronic structure of $(TPP)_2Cu_4I_6{\cdot}2DMSO$.

To further elucidate photophysical properties of $(TPP)_2Cu_4I_6{\cdot}2DMSO$ powders, temperature-dependent PL spectra were measured in the range of 80-370 K (**Figure 3**a). As the temperature increased from 80 to 370 K, a gradual reduction in the PL intensity was observed, concomitant with the red shift of the emission peak and a significant broadening of the PL FWHM. This

observation can be attributed to the thermally activated non-radiative recombination of the emitting state(s), leading to the increased non-radiative relaxation rate and fluorescence quenching.[23] With the temperature rising, the population of high-energy vibrational levels increases, exacerbating the non-radiative relaxation channels of the excited state, and leading to the decrease of emission intensity. The observed red shift of the emission peak can also be explained by the bandgap shrinkage with increasing temperature due to augmented electron−phonon interactions, as was previously observed for other OIMHs.[5a, 24]

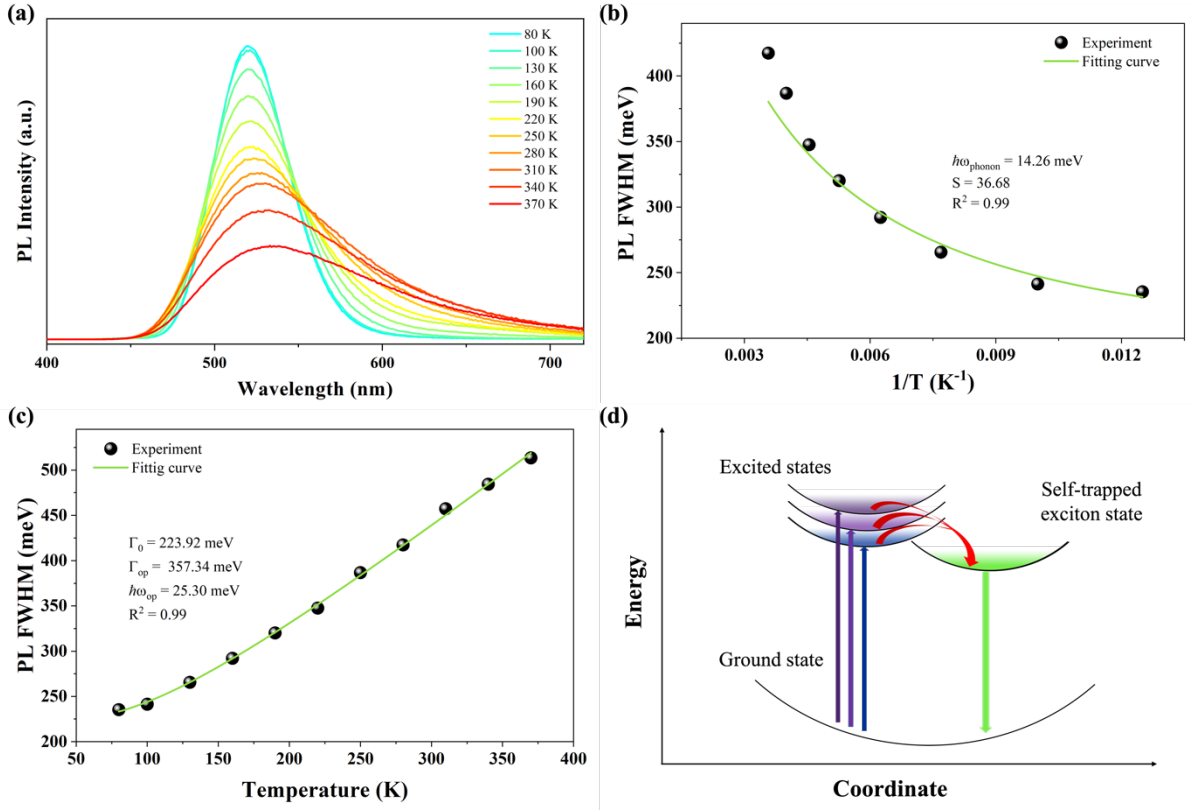

Figure 3. (a) Temperature-dependent PL spectra (λ_{ex} = 370 nm) of the $(TPP)_2Cu_4I_6{\cdot}2DMSO$ powder. Fitting results of the PL FWHM as a function of reciprocal temperature (b) and temperature (c) for the $(TPP)_2Cu_4I_6{\cdot}2DMSO$ powder (see text for details). (d) Schematic illustration of the STE state in $(TPP)_2Cu_4I_6{\cdot}2DMSO$.

For metal halides with their soft lattices, photogenerated electrons in the excited state tend to couple preferentially with lattice vibration, thereby causing transient lattice distortion, resulting in formation of the STE states.[25] We performed a quantitative analysis of the electron-phonon coupling in $(TPP)_2Cu_4I_6{\cdot}2DMSO$ by deriving the Huang–Rhys factor *S* from the temperature-dependent PL spectra. Considering the relationship between reciprocal temperature and *S*, the photon energy ($\hbar\omega_{phonon}$) can be obtained by using the following equation:[26]

$$\mathrm{FWHM(T)} = 2.36\sqrt{S}\hbar\omega_{\mathrm{phonon}}\sqrt{\coth\frac{\hbar\omega_{\mathrm{phonon}}}{2K_b T}} \quad (1)$$

and electron-optical phonon coupling energy and longitudinal optical phonon energy can be acquired from the equation:[27]

$$\Gamma(T) = \Gamma_0 + \frac{\Gamma_{op}}{e^{\hbar\omega_{op}/K_b T}-1} \quad (2)$$

where $\hbar = h/2\pi$ is reduced Planck constant, ω_{phonon} is phonon frequency, T is temperature, K_b is Boltzmann constant, Γ_0 is the FWHM value at absolute temperature 0 K, Γ_{op} is the electron-optical phonon coupling energy, $\hbar\omega_{op}$ is the longitudinal optical phonon energy. As shown in Figure 3b, the emission band broadens with its FWHM increasing from 235.43 meV to 417.35 meV upon increasing temperature from 80 K to 370 K. From Eqs. (1) and (2), this translates into a large S = 36.68 and a phonon energy of the excited state $\hbar\omega_{phonon}$ = 14.26 meV for the $(TPP)_2Cu_4I_6$·2DMSO (Figure 3b). Such value of S is indeed pretty high as compared to other reported luminescent 0D OIMHs,[28] demonstrating the strong electron–phonon coupling and easy formation of STE in the $(TPP)_2Cu_4I_6$·2DMSO compound where $[Cu_4I_6]^{2-}$ polyhedron units act as 0D luminescence centers by trapping excitons. We estimated the exciton self-trapping time to be $\tau = 2\pi/\omega_{phonon}$ = 290 fs, which indicates an ultrafast STE formation. Moreover, the values of Γ_{op} and $\hbar\omega_{op}$ are calculated as 357.34 meV and 25.30 meV, respectively (Figure 3c), which are comparable to other reported 0D OIMHs.[29] Strong electron-optical phonon coupling implies a large lattice distortion of $(TPP)_2Cu_4I_6$·2DMSO, which is the most probable origin of STE. Figure 3d shows a schematic configuration coordinate diagram illustrating the photophysical processes involved in the STE emission mechanism of $(TPP)_2Cu_4I_6$·2DMSO. Upon high-energy excitation, electrons undergo transition from the ground state to excited states, whereas there are three transition channels responsible for the existence of three PLE peaks of $(TPP)_2Cu_4I_6$·2DMSO as illustrated in Figure 2a. Due to the electron-phonon interactions arising from the distortion of $[Cu_4I_6]^{2-}$ polyhedron units, it becomes possible to form a STE state capturing the excitons, ultimately resulting in the observed broad emission of this compound (Figure 2a).

Stability of light-emitting materials is important for any practical application. Quite remarkably, the absolute PL QY of the $(TPP)_2Cu_4I_6$·2DMSO powder showed negligible change (from 99.5% to 98.3% only) after exposure to air for up to 63 days, as shown in Figure S9b (Supporting Information). The emission intensity of the powder was also well maintained for up to 70 days, further confirming its excellent air stability (Figure S12, Supporting Information). Moreover, this compound exhibited good UV stability retaining 90% PL intensity under 365 nm UV light irradiation for up to 100 h (Figure S13, Supporting Information).

2.3 White Light-Emitting Devices

As outlined above, $(TPP)_2Cu_4I_6 \cdot 2DMSO$ possesses a highly efficient luminescence and exhibits a broad excitation spectrum, which qualifies it for the use in down-conversion WLEDs. To demonstrate its applicability as a green phosphor in WLEDs, we fabricated a single component device denoted as WLED1 by coating $(TPP)_2Cu_4I_6 \cdot 2DMSO$ on a commercial 450 nm blue-LED chip. **Figure 4**a shows the emission spectrum of WLED1, with a Commission Internationale de l'Eclairage (CIE) coordinate of (0.26, 0.30) as shown in Figure 4b, and a correlated color temperature (CCT) of 12449 K. The luminous efficiency of this device reached 50 lm W^{-1}, which is much higher than of a filament lamp (roughly 18 lm W^{-1}) and twice of the reported value for a similar compound $[Na(DMSO)_2]_3SbBr_3Cl_3$ pumped by 450 nm blue-LED chip (25.2 lm W^{-1}).[30] A photograph of the working WLED1 device is given in Figure 4c. To produce other WLEDs, we further fabricated two devices by: (i) combination of the blue $Cs_3Cu_2I_5$ + green $(TPP)_2Cu_4I_6 \cdot 2DMSO$ + orange $(TPP)_2SbCl_5$ phosphors coated on a commercial 300 nm UV-LED chip, and (ii) combination of the blue TPPI + green $(TPP)_2Cu_4I_6 \cdot 2DMSO$ + orange $(TPP)_2SbCl_5$ phosphors deposited on a 365 nm UV-LED chip, which we denote as WLED2 and WLED3, respectively. As shown in Figure 4d, the emission spectrum of WLED2 covers the broad range of 400-800 nm, and this device displays a CIE coordinate of (0.33, 0.36) as shown in Figure 4e, with a high color rendering index (CRI) of 94.4 and a CCT of 5563 K. The emission spectrum of WLED3 is also broad, consisting of the combination of peaks from its components (Figure 4g); it shows a CIE coordinate of (0.33, 0.35) as given in Figure 4h, an even higher CRI of 96.7 and a CCT of 5450 K. The photographs of the working devices WLED2 and WLED3 are shown in Figure 4f and 4i, respectively. The above results demonstrate the potential of $(TPP)_2Cu_4I_6 \cdot 2DMSO$ as a promising green phosphor for down-conversion WLEDs achieving tunable CIE coordinates and CCTs.

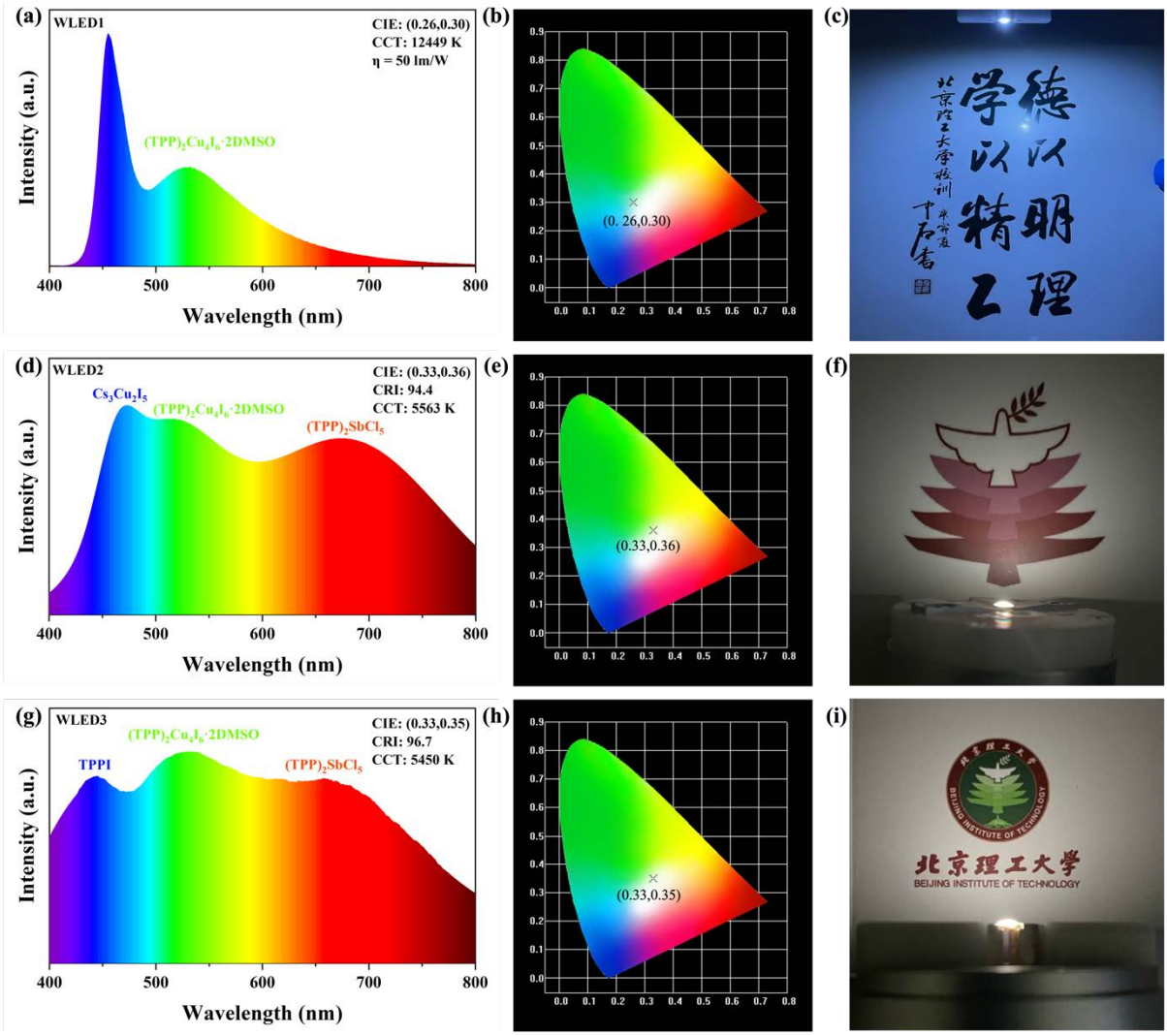

Figure 4. Emission spectra of WLED1 (a), WLED2 (d) and WLED3 (g), and CIE chromaticity diagrams of WLED1 (b), WLED2 (e) and WLED3 (h). Photographs of the working devices WLED1 (c), WLED2 (f) and WLED3 (i).

2.4 Scintillators and Luminescent Inks

$(TPP)_2Cu_4I_6$·2DMSO powder was also used to fabricate a scintillator for X-ray detection and imaging. In order to assess the capabilities of this X-ray scintillator, an X-ray imaging system was built, as illustrated in **Figure 5**a. The fabricated $(TPP)_2Cu_4I_6$·2DMSO scintillator screen (~1mm thickness and ~2 cm in diameter) achieved a spatial resolution of 2.5 lp mm^{-1} (Figure 5b). Notably, as illustrated in Figure 5c, the $(TPP)_2Cu_4I_6$·2DMSO scintillator exhibited a low detection limit of 310 nGy_{air} s^{-1}, which is one magnitude lower than the requirement for X-ray diagnostics (5.5 μGy_{air} s^{-1}).[31] The images of a spring enclosed in a capsule and a copper component were captured under both daylight and X-ray, and all the details inside those

samples could clearly be recognized under X-ray (Figure 5d). As shown in Figure 5e, the integrated scintillation intensity increased linearly with the X-ray dose rate in the range from 1.1 to 6.8 mGy_{air} s^{-1}, which is beneficial for X-ray detection. These findings demonstrate potential of $(TPP)_2Cu_4I_6{\cdot}2DMSO$ in practical X-ray imaging applications such as security checks and medical radiography.

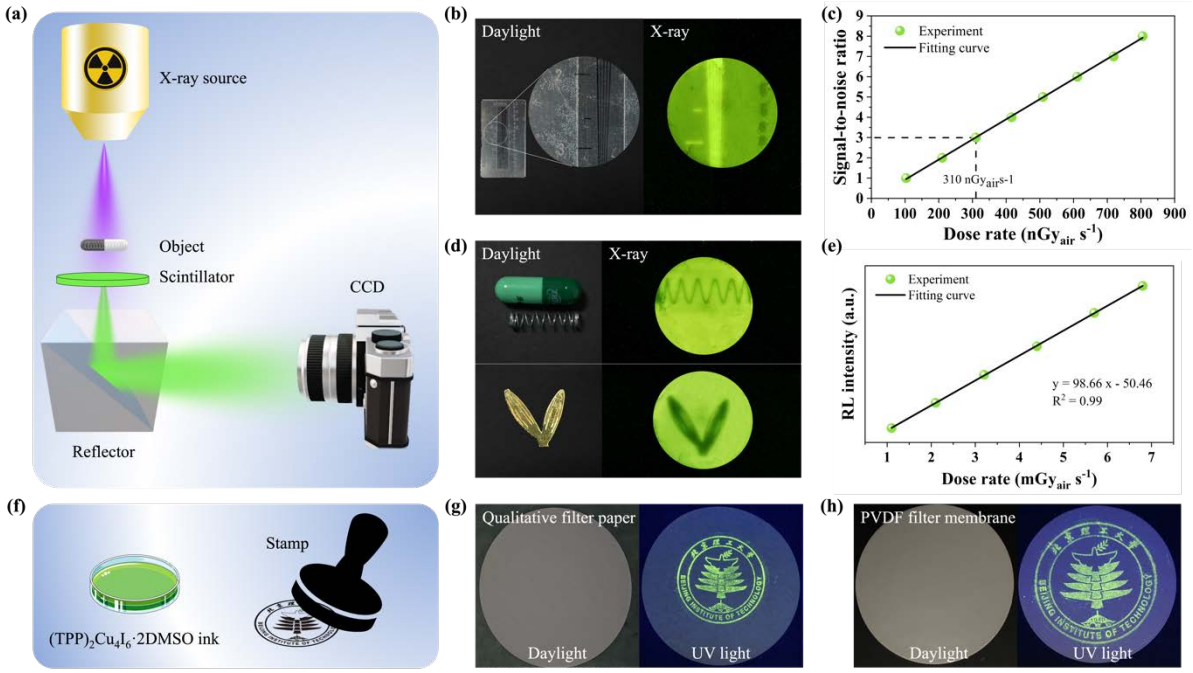

Figure 5. (a) Schematic diagram of the X-ray imaging apparatus used to evaluate the $(TPP)_2Cu_4I_6{\cdot}2DMSO$ scintillator. (b) A line pair card under daylight (left) and X-ray (right) for spatial resolution measurement of the X-ray imaging. (c) Signal-to-noise ratio as a linear function of the X-ray dose rate. (d) Images of a spring in a capsule and a copper component under daylight (left) and X-ray (right). (e) Integrated scintillation intensity as a linear function of the X-ray dose rate. (f) Schematic illustration of the $(TPP)_2Cu_4I_6{\cdot}2DMSO$ luminescent ink, and of a stamp with BIT logo printed using this ink. Photographs of the luminescent BIT logo were taken under daylight (left) and UV light (right), stamp-printed on a filter paper (g) and PVDF filter membrane (h).

To explore the potential use of $(TPP)_2Cu_4I_6{\cdot}2DMSO$ for encryption applications, we employed a conventional contact printing technique. A stamp was custom-fabricated to depict the logo of BIT (Beijing Institute of Technology) as shown in Figure 5f. The $(TPP)_2Cu_4I_6{\cdot}2DMSO$ ink was prepared by mixing $(TPP)_2Cu_4I_6{\cdot}2DMSO$ powder, silicone resin OE-6551A and hardener OE-6551B with a weight ratio of 1:1:2. The luminescent BIT logo was

imprinted on various substrates, such as filter paper, polyvinylidene fluoride (PVDF) filter membrane, kimwipe, glass, and Nylon filter membrane. The imprinted patterns were invisible under daylight, but prominently emitted a bright green light under 365 nm UV light excitation (Figure 5g, h and Figure S14a-c, Supporting Information). In addition to the aforementioned substrates, several other materials were also checked, namely weigh paper, aluminum foil and black cardboard: in those cases, the imprinted patterns were also discernible under daylight (Figure S14d-f, Supporting Information). These results demonstrate the potential use of $(TPP)_2Cu_4I_6{\cdot}2DMSO$ inks in information storage and anti-counterfeiting, where messages could be encrypted and visualized under UV light.

3. Conclusions

Organic-inorganic copper halide compound $(TPP)_2Cu_4I_6{\cdot}2DMSO$ has been successfully synthesized with very high PL QY close to unity. Under UV light excitation, this compound exhibited a bright green broadband emission with a peak at 515 nm, which originates from STE localized on the $[Cu_4I_6]^{2-}$ polyhedron within 0D OIMH. Remarkably, $(TPP)_2Cu_4I_6{\cdot}2DMSO$ also displayed high stability when stored in air and exposed to 365 nm UV light irradiation, making it a promising material for practical applications. The broad excitation spectrum of this compound was beneficial for pumping by commercial blue- and UV-LED chips, which enabled fabrication of down-conversion WLEDs with high CRI. We also demonstrate how $(TPP)_2Cu_4I_6{\cdot}2DMSO$ can be used in X-ray detection/imaging, and as a luminescent ink for information encryption.

4. Experimental Section

Chemicals: All reagents and solvents were purchased and used as received without further purification: copper (I) iodide, (CuI, 98%, Sigma-Aldrich), tetraphenylphosphonium iodide (TPPI, 98%, J&K), dimethyl sulfoxide (DMSO, 99.9%, super-dry, J&K), ethanol (EtOH, 99.7%, Beijing Institute of Chemical Reagent Co., Ltd., China). PVDF microporous filter membrane (0.22 μm, hydrophobic) was obtained from Newstar.

Synthesis of $(TPP)_2Cu_4I_6{\cdot}2DMSO$ single crystals: $(TPP)_2Cu_4I_6{\cdot}2DMSO$ single crystals were produced by cooling crystallization method. TPPI (0.4663 g, 1 mmol) and CuI (0.2856 g, 1.5 mmol) were dissolved in 2 mL DMSO. The solution was heated to 100 ^{o}C under stirring until it became clear. After filtration via a polytetrafluoroethylene filter membrane with pore size of

0.45 μm, the solution was cooled down to room temperature, and $(TPP)_2Cu_4I_6 \cdot 2DMSO$ single crystals with sizes of 1-3 mm were isolated.

Synthesis of $(TPP)_2Cu_4I_6 \cdot 2DMSO$ powder: $(TPP)_2Cu_4I_6 \cdot 2DMSO$ powder was produced by a one-step antisolvent method. TPPI (0.0466 g, 0.10 mmol) and CuI (0.0285 g, 0.15 mmol) were dissolved in 1 mL DMSO under ultrasonication to form a clear solution (the molar ratio of TPPI to CuI here was 1:1.5). Subsequently, 3 mL EtOH was added slowly under vigorous stirring at room temperature. The transparent solution became turbid, indicating formation of $(TPP)_2Cu_4I_6 \cdot 2DMSO$. The same process was adopted for another tested molar ratios (1:1 and 1:2) of TPPI to CuI.

Filter membrane-assisted post-processing: $(TPP)_2Cu_4I_6 \cdot 2DMSO$ powder was extracted from its suspension by syringe, and injected into the filter with PVDF microporous membrane. The powder remained on the filter and has been collected by scrapping.

Fabrication of WLEDs: To produce WLED1, 0.05 g $(TPP)_2Cu_4I_6 \cdot 2DMSO$ powder was mixed with a thermal-curable silicone resin OE-6551A (0.10 g) and a hardener OE-6551B (0.20 g) under vigorous stirring to form a paste, which was coated on a commercial 450 nm blue-LED chip (EPILED Co., Ltd). To produce WLED2, 0.10 g $Cs_3Cu_2I_5$, 0.03 g $(TPP)_2Cu_4I_6 \cdot 2DMSO$ and 0.08 g $(TPP)_2SbCl_5$ powders were thoroughly mixed with the resin OE-6551A (0.10 g) and the hardener OE-6551B (0.20 g) under vigorous stirring. The paste formed was coated a commercial 300 nm UV-LED chip (EPILED Co., Ltd). Blue-emitting $Cs_3Cu_2I_5$[32] and orange-emitting $(TPP)_2SbCl_5$[33] compounds were synthesized according to mentioned literature sources, using grinding method. To produce WLED3, the same procedures were employed, but the amount of the components was changed to 0.15 g TPPI, 0.02 g $(TPP)_2Cu_4I_6 \cdot 2DMSO$ and 0.10 g $(TPP)_2SbCl_5$; the final paste was coated on a commercial 365 nm UV-LED chip (EPILED Co., Ltd).

Fabrication of $(TPP)_2Cu_4I_6 \cdot 2DMSO$ scintillators: 0.5 g of the $(TPP)_2Cu_4I_6 \cdot 2DMSO$ powder was pressed at 15 MPa for 10 min to form a scintillator screen with a thickness of ~1 mm and a diameter of ~2 cm.

Characterization: Single crystal XRD data were collected on a XtaLAB Synergy X-ray diffractometer with Cu-Kα (λ = 1.54184 Å) radiation at 293 K. An empirical multi-scan absorption correction was applied using the CrysAlisPro 1.171.42.60a software package. The SHELXTL 6.14 software package (Bruker) was used to solve and refine crystal structure.[34] The structure was solved by direct methods and refined by the full-matrix least-squares method ($\Sigma w(|F_0|^2 - |Fc|^2)^2$) with anisotropic thermal parameters for all atoms included in the model. The hydrogen atoms of the organic groups were introduced in geometrically calculated positions.

Powder XRD measurements were performed on an X-ray diffractometer (Bruker AXS D8) using Cu-Kα X-ray radiation (λ = 1.5406 Å). Thermo Scientific Apreo 2S equipped with Ultra Dry detector was used to collect SEM images and record the EDS data. XPS data were acquired on a PHI QUANTERA-II SXM from the manufacturer ULVAC-PHI with Al Kα radiation (1486.6 eV, line width below 0.48 eV) as the X-ray source. ICP-OES measurements were performed on an Agilent 5110, and ICP-MS measurements - on an Aglient 7800 (MS). Organic elemental analysis was performed on an Elementar UNICUBE. TGA measurements were done on a METTLER TGA/DSC1 under N_2 atmosphere. FTIR spectra were collected on a Thermo Fisher Nicolet Is10 instrument. Diffuse reflection spectra were collected on a Hitachi UH5700 spectrophotometer equipped with an integrating sphere, using $BaSO_4$ as the reference standard. Steady-state PL and PLE spectra were measured on a Hitachi F7000 equipped with appropriate filters. Absolute PL QYs were recorded on a Hamamatsu Quantaurus-QY. Time-resolved PL decays were measured on an Edinburgh FLS1000 spectrofluorometer. Power-dependent PL measurements were made using a current-tunable LED driver equipped with an integrating sphere. Temperature-dependent PL spectra were obtained on a Horiba Nanolog apparatus equipped with low-temperature accessories. The X-ray imaging system was implemented by combining the W Kα X-ray source and SONY alpha7; its detection limit was measured by a standard photodiode power sensor S120VC from Thorlabs.

Computational Methods: The VASP[35] was employed to perform all the DFT calculations within the generalized gradient approximation (GGA) using the Perdew-Burke-Ernzerhof (PBE)[36] formulation. PAW potentials[37] have been chosen to describe the ionic cores, taking valence electrons into account using a plane wave basis set with a kinetic energy cutoff of 500 eV. The *k*-point mesh was set as a 2×2×2 Monkhorst-Pack grid for Brillouin zone sampling. Partial occupancies of the Kohn−Sham orbitals were allowed using the Gaussian smearing method and a width of 0.05 eV. The electronic energy was considered self-consistent when the energy change was smaller than 10^{-5} eV. A geometry optimization was considered convergent when the energy change was smaller than 10^{-5} eV.

[CCDC 2266272 contains the supplementary crystallographic data for this paper. These data can be obtained free of charge from The Cambridge Crystallographic Data Centre via www.ccdc.cam.ac.uk/data_request/cif.]

Supporting Information

Supporting Information is available from the Wiley Online Library or from the author.

Acknowledgements

This work was supported by the Foundation Enhancement Program (2021-JCJQ-2JJ-0199), Open Foundation of the State Key Laboratory of Featured Metal Materials and Life-Cycle Safety for Composite Structures (2022GXYSOF20), Beijing Goldbridge Project (ZZ22002), Open Foundation of State Key Laboratory of Luminescent Materials and Devices (2023-skllmd-23), the Fundamental Research Funds of Shaanxi Key Laboratory of Artificially-Structured Functional Materials and Devices (AFMD-KFJJ-22102), the financial support program from Hebei Province (Grant No. B2022205028 and C20220322) and the Croucher Foundation of Hong Kong.

Received: ((will be filled in by the editorial staff))
Revised: ((will be filled in by the editorial staff))
Published online: ((will be filled in by the editorial staff))

References

[1] a) Y. Jia, W.-L. Guan, J. Liu, J.-P. Hu, B. Shi, H. Yao, Y.-M. Zhang, T.-B. Wei, Q. Lin, *Chin. Chem. Lett.* **2023**, *34*, 108082; b) J.-W. Lee, S. M. Kang, *Nano-Micro Lett.* **2023**, *15*, 184; c) Y.-J. Li, T.-T. Huang, J. Liu, Y.-Q. Xie, B. Shi, Y.-M. Zhang, H. Yao, T.-B. Wei, Q. Lin, *ACS Sustain. Chem. Eng.* **2022**, *10*, 7907; d) G. Vidon, P. Dally, M. Al-Katrib, D. Ory, M. Kim, E. Soret, E. Rangayen, M. Legrand, A. Blaizot, P. Schulz, J.-B. Puel, D. Suchet, J.-F. Guillemoles, A. Etcheberry, M. Bouttemy, S. Cacovich, *Adv. Funct. Mater.* **2023**, *33*, 2304730.

[2] a) J. Sun, J. Wu, X. Tong, F. Lin, Y. Wang, Z. M. Wang, *Adv. Sci.* **2018**, *5*, 1700780; b) N. K. Noel, S. D. Stranks, A. Abate, C. Wehrenfennig, S. Guarnera, A.-A. Haghighirad, A. Sadhanala, G. E. Eperon, S. K. Pathak, M. B. Johnston, A. Petrozza, L. M. Herz, H. J. Snaith, *Energy Environ. Sci.* **2014**, *7*, 3061; c) Z. Wan, *J.Mater. Res.* **2020**, *35*, 2166; d) F. Sani, S. Shafie, H. N. Lim, A. O. Musa, *Materials* **2018**, *11*, 1008.

[3] a) S. Fang, H. Li, Y. Xie, H. Li, Y. Wang, Y. Shi, *Small* **2021**, *17*, 2103831; b) C. Li, Z. Luo, Y. Liu, Y. Wei, X. He, Z. Chen, L. Zhang, Y. Chen, W. Wang, Y. Liu, X. Chang, Z. Quan, *Adv. Opt. Mater.* **2022**, *10*, 2102746; c) S.-H. He, J. Zhao, Q.-L. Liu, *Chinese J. Inorg. Chem.* **2022**, *38*, 1209; d) H.-K. Seo, H. Kim, J. Lee, M.-H. Park, S.-H. Jeong, Y.-H. Kim, S.-J. Kwon, T.-H. Han, S. Yoo, T.-W. Lee, *Adv. Mater.* **2017**, *29*, 1605587; e) L. Fan, K. Liu, Q. Zeng, M. Li, H. Cai, J. Zhou, S. He, J. Zhao, Q. Liu, *Acs Appl. Mater. Inter.* **2021**, *13*, 29835; f) J. Cao, J. Lin, K. Liu, Y. Xiong, N. Wang, S. He, X. Zhang, Z. Guo, X. Chen, J. Zhao, Q. Liu, *J. Mater. Chem. C* **2022**, *10*, 9841.

[4] a) L. Yao, X. Fang, D. Fang, C. Gao, S. Liu, R. Li, D. Wang, Z. Wei, X. Wang, *Acta Photonica Sinic.* **2021**, *50*, 26; b) B.-S. Zhu, Z. He, J.-S. Yao, C. Chen, K.-H. Wang, H.-B. Yao, J.-W. Liu, S.-H. Yu, *Adv. Opt. Mater.* **2018**, *6*, 1701029; c) Z. Zhang, S. Yang, J. Hu, H. Peng, H. Li, P. Tang, Y. Jiang, L. Tang, B. Zou, *Nanoscale* **2022**, *14*, 4170; d) S. Tong, H. Wu, C. Zhang, S. Li, C. Wang, J. Shen, S. Xiao, J. He, J. Yang, J. Sun, Y. Gao, *Org. Electron.* **2017**, *49*, 347; e) T. Liu, W. Tang, S. Luong, O. Fenwick, *Nanoscale* **2020**, *12*, 9688.

[5] a) H. Peng, Y. Tian, X. Wang, T. Huang, Z. Yu, Y. Zhao, T. Dong, J. Wang, B. Zou, *ACS Appl. Mater. Inter.* **2022**, *14*, 12395; b) S. Zhu, J. Pan, X. Chen, H. Chen, S. Pan, *J. Lumin.* **2023**, *253*, 119467.

[6] X. Meng, S. Ji, Q. Wang, X. Wang, T. Bai, R. Zhang, B. Yang, Y. Li, Z. Shao, J. Jiang, K.-l. Han, F. Liu, *Adv. Sci.* **2022**, *9*, 2203596.

[7] a) X. Zhang, W. Liu, G. Z. Wei, D. Banerjee, Z. Hu, J. Li, *J. Am. Chem. Soc.* **2014**, *136*, 14230; b) L. Zhang, R. Shi, H. Qiu, X. Jiang, G. Sun, R. Long, W. H. Fang, *J. Phys. Chem. Lett.* **2022**, *13*, 11936.

[8] a) S. S. Das, A. Pradhan, S. L. Samal, *Dalton T.* **2023**, *52*, 1777; b) Q. Mo, J. Yu, C. Chen, W. Cai, S. Zhao, H. Li, Z. Zang, *Laser Photonics Rev.* **2022**, *16*, 2100600.

[9] a) H. Lin, C. Zhou, J. Neu, Y. Zhou, D. Han, S. Chen, M. Worku, M. Chaaban, S. Lee, E. Berkwits, T. Siegrist, M.-H. Du, B. Ma, *Adv. Opt. Mater.* **2019**, *7*, 1801474; b) J. Kundu, D. K. Das, *Eur. J. Inorg. Chem.* **2021**, *2021*, 4508.

[10] a) A. Jana, C. W. Myung, V. G. Sree, K. S. Kim, *Mater. Chem. Front.* **2022**, *6*, 3102; b) C. Zhou, H. Lin, H. Shi, Y. Tian, C. Pak, M. Shatruk, Y. Zhou, P. Djurovich, M.-H. Du, B. Ma, *Angew. Chem. Int. Ed.* **2018**, *57*, 1021; c) X. Liu, Y. Li, T. Liang, J. Fan, *J. Phys. Chem. Lett.* **2021**, *12*, 5765.

[11] Y. Li, Z. Zhou, F. K. Sheong, Z. Xing, K. S. Wong, H. H. Y. Sung, I. D. Williams, J. E. Halpert, *Chem. Mater.* **2023**, *35*, 1318.

[12] Y. Li, Z. Zhou, F. K. Sheong, Z. Xing, R. Lortz, K. S. Wong, H. H. Y. Sung, I. D. Williams, J. E. Halpert, *ACS Energy Lett.* **2021**, *6*, 4383.

[13] a) S. Zhou, Y. Chen, K. Li, X. Liu, T. Zhang, W. Shen, M. Li, L. Zhou, R. He, *Chem. Sci.* **2023**, *14*, 5415; b) R. Roccanova, M. Houck, A. Yangui, D. Han, H. Shi, Y. Wu, D. T. Glatzhofer, D. R. Powell, S. Chen, H. Fourati, A. Lusson, K. Boukheddaden, M.-H. Du, B. Saparov, *ACS Omega* **2018**, *3*, 18791.

[14] a) B. Wang, C. Chen, X. Yang, W. Cai, S. Zhao, R. Li, W. Ma, J. Chen, Z. Zang, *EcoMat* **2022**, *4*, e12184; b) H. Peng, X. Wang, Y. Tian, B. Zou, F. Yang, T. Huang, C. Peng, S. Yao, Z. Yu, Q. Yao, G. Rao, J. Wang, *ACS Appl. Mater. Inter.* **2021**, *13*, 13443.

[15] L. Lian, P. Zhang, G. Liang, S. Wang, X. Wang, Y. Wang, X. Zhang, J. Gao, D. Zhang, L. Gao, H. Song, R. Chen, X. Lan, W. Liang, G. Niu, J. Tang, J. Zhang, *ACS Appl. Mater. Inter.* **2021**, *13*, 22749.

[16] a) R. Lin, Q. Guo, Q. Zhu, Y. Zhu, W. Zheng, F. Huang, *Adv. Mater.* **2019**, *31*, 1905079; b) W. E. Swartz, J. K. Ruff, D. M. Hercules, *J. Am. Chem. Soc.* **1972**, *94*, 5227.

[17] a) Y. Thefioux, M. Cordier, F. Massuyeau, C. Latouche, C. Martineau-Corcos, S. Perruchas, *Inorg. Chem.* **2020**, *59*, 5768; b) B. Haddad, A. Paolone, D. Villemin, M. Taqiyeddine, E.-h. Belarbi, S. Bresson, M. Rahmouni, N. R. Dhumal, H. J. Kim, J. Kiefer, *J. Mol. Struct.* **2017**, *1146*, 203.

[18] a) C.-Q. Jing, Q.-L. Liu, C.-H. Zhao, Y.-Y. Zhao, C.-Y. Yue, X.-W. Lei, *J. Mater. Chem. C* **2021**, *9*, 15047; b) H. Peng, X. Wang, Y. Tian, T. Dong, Y. Xiao, T. Huang, Y. Guo, J.

Wang, B. Zou, *J. Phys. Chem. Lett.* **2021**, *12*, 6639; c) Z. Wang, Z. Zhang, L. Tao, N. Shen, B. Hu, L. Gong, J. Li, X. Chen, X. Huang, *Angew. Chem. Int. Ed.* **2019**, *58*, 9974; d) L.-J. Xu, X. Lin, Q. He, M. Worku, B. Ma, *Nat. Commun.* **2020**, *11*, 4329.

[19] Z. Ma, X. Ji, S. Lin, X. Chen, D. Wu, X. Li, Y. Zhang, C. Shan, Z. Shi, X. Fang, *Adv. Mater.* **2023**, *35*, 2300731.

[20] T. Schmidt, K. Lischka, W. Zulehner, *Phys. Rev. B* **1992**, *45*, 8989.

[21] D. Chen, S. Hao, G. Zhou, C. Deng, Q. Liu, S. Ma, C. Wolverton, J. Zhao, Z. Xia, *Inorg. Chem.* **2019**, *58*, 15602.

[22] F. Liu, D. Mondal, K. Zhang, Y. Zhang, K. Huang, D. Wang, W. Yang, P. Mahadevan, R. Xie, *Mater. Adv.* **2021**, *2*, 3744.

[23] R. Gautier, M. Paris, F. Massuyeau, *J. Am. Chem. Soc.* **2019**, *141*, 12619.

[24] C. Zhou, H. Lin, J. Neu, Y. Zhou, M. Chaaban, S. Lee, M. Worku, B. Chen, R. Clark, W. Cheng, J. Guan, P. Djurovich, D. Zhang, X. Lu, J. Bullock, C. Pak, M. Shatruk, M.-H. Du, T. Siegrist, B. Ma, *ACS Energy Lett.* **2019**, *4*, 1579.

[25] R. Zeng, K. Bai, Q. Wei, T. Chang, J. Yan, B. Ke, J. Huang, L. Wang, W. Zhou, S. Cao, J. Zhao, B. Zou, *Nano Res.* **2021**, *14*, 1551.

[26] W. Stadler, D. M. Hofmann, H. C. Alt, T. Muschik, B. K. Meyer, *Phys. Rev. B* **1995**, *51*, 10619.

[27] R. Zeng, L. Zhang, Y. Xue, B. Ke, Z. Zhao, D. Huang, Q. Wei, W. Zhou, B. Zou, *J. Phys. Chem. Lett.* **2020**, *11*, 2053; b) M. Sebastian, J. A. Peters, C. C. Stoumpos, J. Im, S. S. Kostina, Z. Liu, M. G. Kanatzidis, A. J. Freeman, B. W. Wessels, *Phys. Rev. B* **2015**, *92*; c) Y. Toyozawa, *Prog. Theor. Phys.* **1962**, *27*, 89.

[28] a) S. Fang, A. Du, B. Zhou, Z. Liu, J. Nie, Y. Wang, H. Zhong, H. Hu, H. Li, Y. Shi, *Adv. Opt. Mater.* **2023**, *11*, 2202952; b) R. He, M. Li, Y. Chen, L. Zhou, S. Zhou, D. You, H. Xiong, Y. Hu, Q. Chen, *Inorg. Chem.* **2023**, *62*, 2806.

[29] a) L. Zhou, J. F. Liao, Z. G. Huang, J. H. Wei, X. D. Wang, H. Y. Chen, D. B. Kuang, *Angew. Chem. Int. Ed.* **2019**, *58*, 15435; b) B. Su, M. Li, E. Song, Z. Xia, *Adv. Funct. Mater.* **2021**, *31*, 2105316.

[30] Q. Mo, Q. Qian, Y. Shi, W. Cai, S. Zhao, Z. Zang, *Adv. Opt. Mater.* **2022**, *10*, 2201509.

[31] S. Y. Yao, H. Li, M. Zhou, T. C. Wang, X. Yu, Y. S. Xu, J. H. Yi, J. B. Qiu, J. Yu, X. H.Xu, *ACS Appl. Mater. Inter.* **2022**, *14*, 56957.

[32] L. Xie, B. Chen, F. Zhang, Z. Zhao, X. Wang, L. Shi, Y. Liu, L. Huang, R. Liu, B. Zou, Y. Wang, *Photonics Res.* **2020**, *8*, 768.

[33] A. Ben-Akacha, C. K. Zhou, M. Chaaban, D. Beery, S. Lee, M. Worku, X. S. Lin, R. Westphal, B. W. Ma, *ChemPhotoChem* **2021**, *5*, 326.

[34] G. Sheldrick, *Acta Crystallogr. Sect. C-Struct. Chem.* **2015**, *71*, 3.

[35] a) G. Kresse, J. Furthmuller, *Comp. Mater. Sci.* **1996**, *6*, 15; b) G. Kresse, J. Furthmuller, *Phys. Rev. B* **1996**, *54*, 11169.

[36] J. P. Perdew, K. Burke, M. Ernzerhof, *Phys. Rev. Lett.* **1997**, *78*, 1396.

[37] a) G. Kresse, D. Joubert, *Phys. Rev. B* **1999**, *59*, 1758; b) P. E. Blochl, *Phys. Rev. B* **1994**, *50*, 17953.

TOC text

We synthesized a novel Cu(I)-based organic-inorganic halide compound $(TPP)_2Cu_4I_6 \cdot 2DMSO$, which exhibits broadband green emission with a near-unity photoluminescence quantum yield; self-trapped excitons are responsible for this emission. This compound was used for fabrication of down-conversion white LEDs, X-ray scintillators and luminescent inks.

TOC figure